Optical Recording System Based on a Fiber Optic Image Conduit: Assessment of Microscopic Activation Patterns in Cardiac Tissue

Stephan Rohr and Jan P. Kucera
Department of Physiology, University of Bern, CH-3012 Bern, Switzerland

ABSTRACT Optical recording of transmembrane voltage changes with the use of potentiometric dyes has opened the possibility of determining spatial patterns of electrical activity in excitable tissues. To follow such activation patterns on the cellular/subcellular level in heart cell cultures, a recording system was developed that features both high spatial resolution (4–200 μm) and high temporal resolution (uncertainty in the determination of delays between fast rising signals of ± 1 μs). Central to the system is a fiber optic image conduit consisting of 379 individual optical fibers. At one end the fibers are fused to form an input window that matches the size of the field of view of the microscope. At the other end, the fibers are loose, permitting a selectable subset to be connected to 80 discrete photodetectors. This design allows the sensitive area of the imager to be adapted to regions of interest in a given preparation, thus making optimal use of the limited number of detectors. Furthermore, by using a second fiber optic imager, individual photodetectors can be assigned to different optical ports, thus providing the means for fast and simultaneous dual-emission wavelength measurements. This feature permitted the elimination of motion artifacts arising from the myocytes without the use of contraction-suppressing drugs.

INTRODUCTION

Since the first use of voltage-sensitive dyes for the assessment of spatial patterns of electrical activation of excitable tissues, several reports have described the design of optical recording devices suitable for the detection of low-level signals generated by these indicators (for a review, cf. Grinvald et al., 1988; Kamino, 1991; Rohr, 1995). Depending on the type of photodetectors used, these systems offered either high pixel counts (CCD cameras) or high temporal resolution (photodiode arrays). CCD cameras were used, e.g., for recording macroscopic activation in cardiac (Gray et al., 1995) or neuronal (Iijima et al., 1996) tissues. These devices are suited to measurements on a macroscopic scale because 1) fluorescence changes are relatively large, because many stacked cell layers contribute to the signal, and 2) propagation times are relatively long, thereby permitting the determination of activation patterns at the slow frame rates typical for these devices (60 Hz; Gray et al., 1995). Both of these features of macroscopic recordings (i.e., large signals and long propagation times) are absent during microscopic determinations of conduction in cultured heart cells: cells form a monolayer producing minimal fluorescence and, if recordings are performed at high spatial resolution, the frame rates of even the fastest CCD cameras currently available (<2 kHz; Iijima et al., 1996) are too slow to accurately follow propagated activation at the cellular level. Under these circumstances, detectors with a higher temporal resolution have to be used. Such devices are typically based on arrays of photodiodes, in which the signals of all detectors are individually amplified and read out in parallel. Typically, photodiode arrays are fabricated on a single chip with pixel counts ranging up to 34 × 34 (Hirota et al., 1995). Alternatively, they consist of many individual photodiodes rigidly coupled to optical fibers that form the input window of the detector (Chien and Pine, 1991). Although these detectors have a low pixel count compared to CCD cameras, they can be operated at much higher frame rates, thus permitting the accurate tracking of microscopic activation.

We describe here the development of a new recording system intended to combine the speed advantage of photodiodes with the possibility of obtaining high-resolution measurements in regions of interest in a given preparation. In particular, the aims of the development were fivefold: 1) design of a device that permits the arrangement of a limited number of detectors according to the shape of a region of interest, thus increasing the local pixel count by an optimization of available resources, i.e., photodetectors; 2) use of a modular structure permitting the straightforward upgrade of the number of photodetectors and/or the maximum pixel count; 3) design of detectors with identical temporal responses to permit the accurate tracking of propagated activation on a subcellular scale; 4) design of low noise detectors to permit single-shot recordings with sufficient signal-to-noise ratios at low light levels; 5) incorporation of the capability to perform fast dual emission measurements.

In its present form, the recording system consists of 80 modularly arranged photodetectors that are coupled to the image plane of a microscope by means of a freely selectable subset of fibers from a hexagonal array of 379 optical fibers. Upgrading the number of detectors is straightforward, and subsets of detectors can be assigned to different ports of the microscope. The system was successfully used to determine activation patterns in monolayer cultures of neonatal rat

---

Received for publication 20 September 1997 and in final form 27 April 1998.

Address reprint requests to Dr. Stephan Rohr, Department of Physiology, University of Bern, Bühlplatz 5, CH-3012 Bern, Switzerland. Tel.: +41-31-631-87-02; Fax: +41-31-631-46-11; E-mail: rohr@pyl.unibe.ch.

0006-3495/98/08/1062/14 $2.00

heart cells with spatial resolutions ranging from 4 μm to 200 μm. Furthermore, using a dual-emission wavelength approach, it was possible to completely eliminate motion artifacts arising from the contraction of myocytes.

MATERIALS AND METHODS

Patterned growth myocyte cultures

Patterned growth monolayer cultures from neonatal rat ventricular myocytes were prepared according to previously published procedures (Rohr et al., 1991; Rohr and Kucera, 1997). The tissue structures, which were produced by photolithographic techniques, consisted of either linear cell strands (10 mm long, 50–70 μm wide) or Y-shaped bifurcations (overall length 2.6 mm, 50 μm wide).

Optical recording system

Optics

The optical part of the setup, as shown schematically in Fig. 1 *A*, was built around an inverted microscope equipped for epifluorescence (Axiovert 135 M; Zeiss, Zürich, Switzerland). The excitation light was provided by a 150-W short arc xenon lamp, which was connected to a low ripple power supply (Optiquip, New York). Light exposure was controlled by a shutter (D122; Vincent Associates, Rochester, NY), which was spring-suspended to minimize vibrations. The excitation light was deflected toward the microscope objectives (Fluar 5×, N.A. 0.25; Fluar 10×, N.A. 0.5; Fluar 20×, N.A. 0.75; Fluar 40×, N.A. 1.3; Plan-Apochromat 100×, N.A. 1.4, all from Zeiss) by a dichroic mirror after passing a cutoff filter. The emitted light was passed through a cut-on filter and the optical coupler (OC) (cf. below) and then projected onto the faceplate of the fiber optic image conduit. In some experiments, optical magnification was increased beyond the specifications of the objectives by the built-in magnifying lenses of the microscope (additional magnification by a factor of 1.6× or 2.5×).

The custom-built OC (Figs. 1 *A* and 2 *B*) mounted on the bottom port of the microscope permitted the simultaneous attachment of up to three imaging devices. It consisted of two vertically stacked sliders, each of which offered three positions for the insertion of optical elements into the light path. The upper slider facing the CCD camera (Sony XC 77CE; Sony Corp., Paramus, NJ) connected to a framegrabber (DT 3152; Data Translation, Marlboro, MA) permitted either a full (silver mirror) or a 50% (cube beamsplitter) intensity picture of the preparation to be recorded. To obtain images of the entire field of view of the microscope, a fiber optic taper was attached to the CCD sensor (Schott, PCO-Computer Optics, Kehlheim, Germany), which reduced the size of the field of view by a factor of 4. The third position of the upper slider was empty, allowing all light to reach the

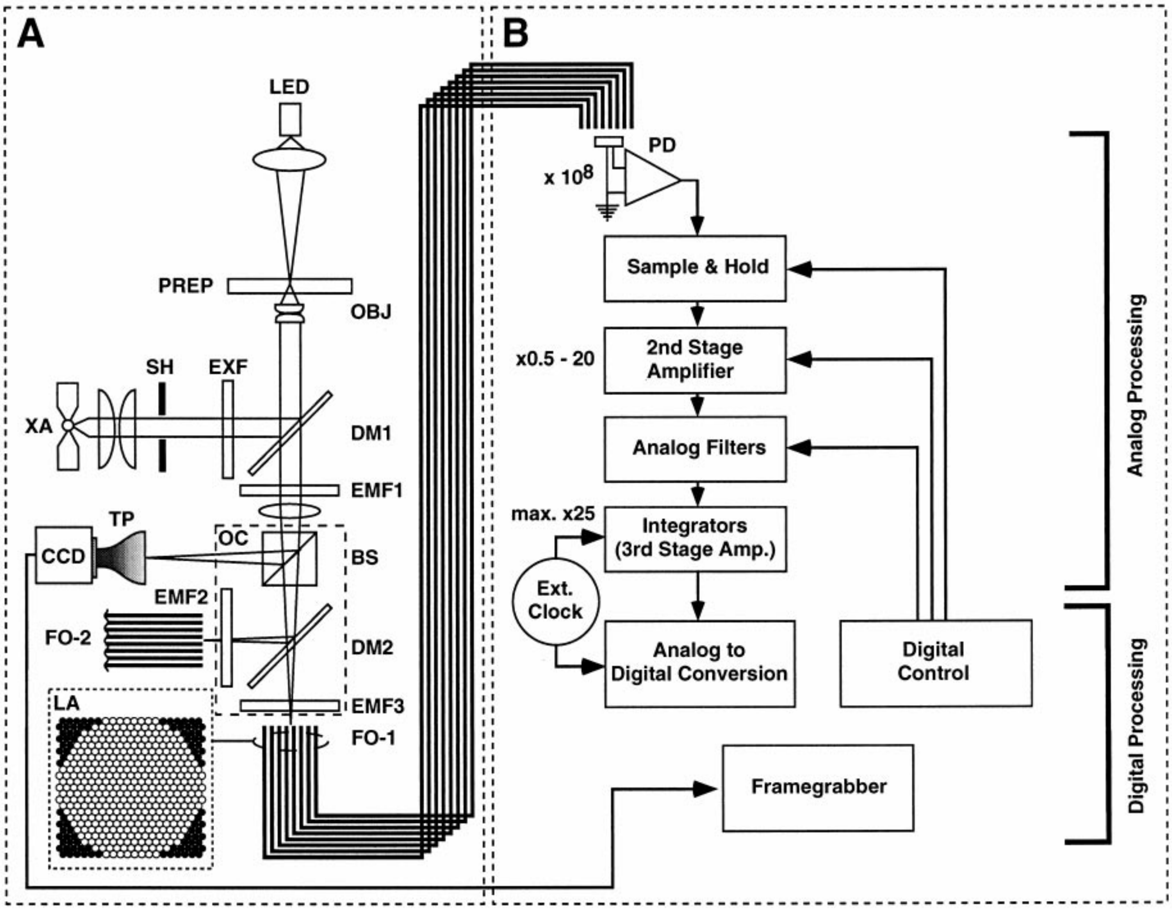

FIGURE 1 Schematic drawing of the components of the optical recording setup. (*A*) Schema of the system optics. (*B*) Chart of the system electronics (for detailed description see text). LED, Light-emitting diode; PREP, preparation; OBJ, objective; XA, xenon arc lamp; SH, shutter; EXF, excitation filter; DM1, first dichroic mirror; EMF1, first emission filter; OC, optical coupler; BS, cube beam splitter; CCD, video camera; TP, fiber optic taper; DM2, second dichroic mirror; EMF2, second emission filter; EMF3, third emission filter; FO-1, primary fiber optic array; FO-2, secondary fiber optic array; LA, spatial arrangement of fibers in the faceplate of the fiber optic array (*white discs*, light-conducting fibers; *black discs*, dummy fibers); PD, photodiode.

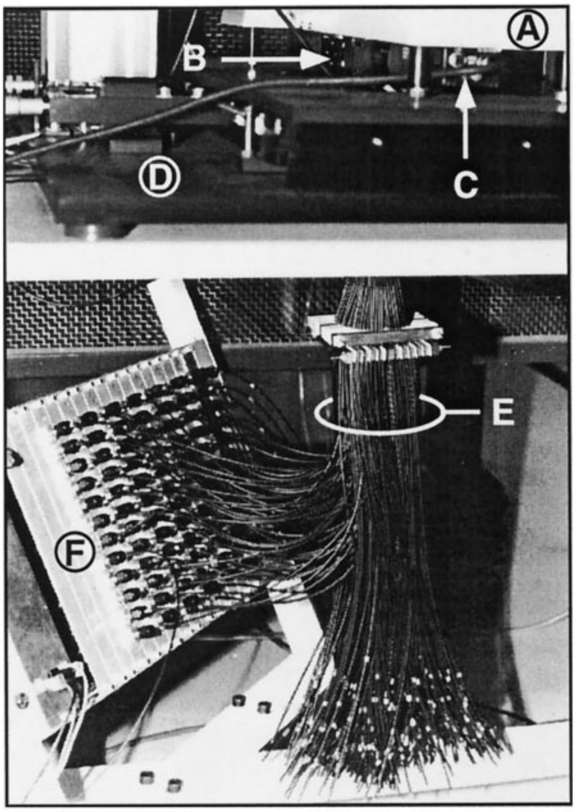

FIGURE 2 Photograph of the optical recording system. The inverted microscope (*A*) is mounted on a motorized *x-y* table (*D*), and the optical coupler (*B*) with its attached CCD camera (*C*) are connected to the optical port at the bottom of the microscope. Below the vibration isolation table, a selection of 80 of the total of 379 optical fibers (*E*) is connected to individual photodetectors in the amplifier rack (*F*).

slider below. There, three combinations of dichroic mirrors and emission filters permitted the recording of separated wavelengths by the two attached fiber optic imagers. All light-deflecting elements in the sliders were fixed on gimbal mounts, facilitating their exact alignment in the light path.

Fiber optic array

During optical recordings, the emitted fluorescence from the preparation was relayed to the photodiodes by a custom-built hexagonal array of 379 plastic fiber optic cables (1-mm-diameter fibers, each polyethylene jacketed: Toray Type PG-U-CD1001, Meteor Optics, Plymouth, MN). A schematic drawing of the layout of the hexagonal array is depicted in Fig. 1 *A* (drawing LA). The fabrication of this array involved the following steps: 1) Individual fibers (∼70 cm long) were dismantled at one end over a distance of 15 cm and were preassembled, row by row. Each row consisted, alternately, of 20 or 21 laterally adjoined fibers, in which the positions not belonging to the imaging hexagon were occupied by 15-cm-long dummy fibers (*black discs* in Fig. 1 *A*, drawing LA). Each row was mechanically fixed in a custom-built holder while the fibers were glued together at either end of the dismantled area with a standard two-component epoxy. 2) The rows of fibers were placed in a U-shaped perspex jig milled exactly to the final dimensions of the densely packed fiber block, and a roof plate was firmly screwed on top of this jig. The jig-fiber assembly was then cast in blackened epoxy under vacuum. 3) The tip of the assembly was cut away between the two regions, where the fibers had initially been glued together (cf. step 1). Then both the exposed faceplate of the array and the loose ends of the fibers, which had been dismantled over a distance of 2 mm, were manually polished. After the fiber optic array was attached to the OC, its position relative to the field of view of the microscope was determined as follows. The loose ends of four peripheral fibers were connected to light-emitting diodes (LEDs) and their output was recorded, after being reflected from a sheet of aluminum placed in the object plane of the microscope, by the CCD camera facing the 50% beamsplitter. The resulting four light spots determined directly the position of the fiber optic array within the field of view of the microscope. The same procedure was also used for the congruent alignment of two fiber optic arrays during dual-emission wavelength experiments; in that case, corresponding fibers in the two arrays were illuminated, and the alignment process was tracked by the CCD camera.

Electronics

As depicted schematically in Fig. 1 *B*, the optical fibers were connected to individual photodiodes (S2164; Hamamatsu, Wissous, France), and the photocurrents were converted to voltages by first-stage amplifiers (OPA121KU; Burr-Brown, Rüschlikon, Switzerland), using a feedback resistor of $100\ \mathrm{M\Omega}$ (gain $= 10^8$ V/A). A fine teflon-insulated wire soldered to one terminal of the resistor acted as an adjustable stray capacitance and served to adjust the time constant of the current-to-voltage converter (IVC) to 100 μs ($f_o = 1.6$ kHz). The IVCs were mounted in individual brass casings, where one end was designed as a light-tight connector permitting the reversible fixation of the optical fibers to the photodiodes (cf. Fig. 2 *F*). The signals from the IVCs were routed to sample and hold (S&H) amplifiers for subtraction of background fluorescence. Thereafter, they were fed to second-stage amplifiers (additional gain of 0.5, 1, 2, 5, or 20×), using either a DC or an AC coupling mode (time constants for AC coupling of 60 ms, 750 ms or 9 s), and were passed through RC low-pass filters (f_o of 0.5, 1, 2, or 3 kHz) to the final amplification stages consisting of integrators (ACF2101BP; Burr-Brown) whose gain was inversely proportional to their driving frequency (additional gain of 25× at 20 kHz). The outputs of the integrators were fed to S&H stages, which conserved the signals during the scanning cycle of the analog-to-digital converters (ADCs). The detectors and their circuitries were mounted in groups of 12 on printed circuit boards, which were connected to a digital control bus. This modular design permitted the upgrading of the total number of channels by simply adding additional boards to the bus. The signals of the 80 detectors were acquired by two 12-bit ADCs (PC20501C; Burr-Brown; installed in a personal computer: Datagate, 133 MHz Pentium; Datacomp, Zürich, Switzerland), which scanned 40 channels, each at a frame rate of 20 kHz. Because the signal conversion was initiated with the clock driving the integrators, all signals recorded originated at exactly the same time, thus establishing a simultaneous sampling system.

Digital control of the experiments

All hardware settings of a given experiment were digitally controlled by protocols describing the timing and/or value of the following variables: 1) mode of stimulation of preparations (rate, timing, selection of electrode); 2) control of optical system (light-emitting diode, LED, and shutter timing); 3) control of electronic components (gain, coupling mode, filter settings, timing of S&H activations, timing and duration of data acquisition, recordings of dark and fluorescence intensities).

Positioning

As shown in Fig. 2, the microscope with all attached devices was mounted on a custom-built *x-y* table. A fixed aluminum frame served to mount the preparation and the stimulation electrodes. This configuration ensured a stable placement of the electrodes with respect to the preparation while permitting free optical scanning of the preparation by movement of the microscope. The microscope was positioned either manually or by stepper motors connected to the *x-y* table. The control unit of the motors (Multicontrol 2000; Märzhäuser, Wetzlar, Germany) was linked to a joystick or, via a serial interface, to a personal computer. Linking to the computer permitted the storing of sites of interest in a preparation for later recalls with a repositioning accuracy of ±2 μm.

Experimental protocol

Typical experimental protocols have been described in detail previously (Rohr and Kucera, 1997). In short, the preparations were mounted in a temperature-controlled chamber (Rohr, 1986) and were superfused with Hanks' balanced salt solution at 36°C (HBSS) (Gibco, Basel, Switzerland; pH 7.40, stabilized with 10 mM HEPES). Then a region of interest was identified and one or two extracellular stimulation electrodes were positioned at a distance greater than 1 mm from the prospective optical recording site. After establishment of successful stimulation (1-ms-long DC pulses at twice threshold intensity), superfusion was stopped and the preparations were stained with 135 μM of the voltage-sensitive dye di-8-ANEPPS, 3-(4-(2-(6-(dioctylamino)-2-naphtyl)-trans-ethenyl)pyridinium)propanesulfonate (Molecular Probes, Eugene, OR) in HBSS for 3–4 min. Thereafter, superfusion was resumed and experiments were started after an equilibration period of 10 min. Fig. 3 shows the diagram of a typical digital control protocol as output by the computer for each experiment. In this graph, the sequential enabling of different hardware components is denoted by lines going high (*shaded in gray*). The actual experimental recording was preceded by a series of tests (phases A and B) aimed at verifying the proper functioning of the system and at evaluating basic experimental parameters. In phase A (test of amplifier frequency response with an LED pulse), the gain, coupling mode, and frequency response were set to the same values used during the experimental recording, and a pulse (trigger 1) started the oscilloscope. The LED was lit and the S&H amplifiers were activated to set the output voltages to zero. Thereafter, digitization was started and the LED was turned off. This resulted in a signal that simulated a simultaneous action potential upstroke (= decreasing fluorescence) for all detectors. As discussed in detail in the Results, this signal was used to generate a temporal correction matrix for all detectors, thus eliminating any inaccuracies left from the stray capacity adjustment (cf. above). In phase B (determination of resting fluorescence), the gain was set to the lowest value to prevent saturation of the amplifiers, and the shutter was opened for a short time. Signals were zeroed by activating the S&H amplifiers, and a single-value digitization was performed. Thereafter, the shutter was closed and a further value (dark value) was acquired. The difference between these two recordings determined the resting fluorescence at each detector and served to calculate fractional fluorescence changes (dF/F) during the experiment. In phase C (experiment) the shutter was opened again, and the gain, coupling mode, and frequency response of the amplifiers were set to the desired values. Thereafter, signals were zeroed by activating the S&H amplifiers, and continuous digitization was started. In this particular experiment, a single stimulation electrode was then activated by a pulse on trigger line 2 and, after a total of 140 ms, the experiment was terminated. The recordings of the experiment controlled by this particular protocol are shown in the Results (Fig. 4 *B*).

Data analysis

The menu-driven data analysis program was written in IDL (Interactive Data Language; Creaso GmbH, Gilching, Germany) and consisted of three main parts: data selection, data processing, and data display:

1. Data selection: When the data of an experiment were loaded, the signals were passed through a digital low-pass filter (f_o from 0.1 to 10 kHz) before being displayed according to their recording location within the field of view of the microscope. This spatial representation permitted the definition of regions of interest for further analysis. A temporal display showing all selected signals in overlaid form was then used to extract regions of the traces that were not contaminated by the motion artifact.

2. Data processing: The amplitudes of the selected signals were scaled either to themselves or to a previous data set, and the following parameters were evaluated for each recording site: signal amplitude, dV/dt_{max}, at_{50} (activation time determined as the point in time when the signal reached 50% of its maximum amplitude; cf. Rohr and Salzberg, 1994b), $at_{dV/dtmax}$ (activation time determined as the time of occurrence of the maximum upstroke velocity), background light intensity, fluorescence intensity, fractional fluorescence change (dF/F), and the characteristics of the test LED pulse (amplitude, dV/dt_{max}, at_{50}).

3. Data display: To facilitate the quick analysis of the results during an ongoing experiment, a number of display options were implemented. Two-dimensional graphs permitted the inspection of the signals and the visualization of the parameters evaluated as a function of time. Isochrones of activation were calculated from the discretely spaced recording sites by triangulation and bilinear interpolation. Furthermore, all of the spatial data representations could be overlaid on the images of the preparations to facilitate a direct correlation between structure and function. Finally, three-dimensional graphs offered the possibility of visualizing parameters of interest according to their recording locations, and the animation of activation permitted the visualization of complex activation patterns.

RESULTS

Impulse propagation in branching cardiac tissue structures

Fig. 4 shows an example of an optical recording in which the possibility of arranging the detectors according to the shape of a given preparation permitted us to obtain a de-

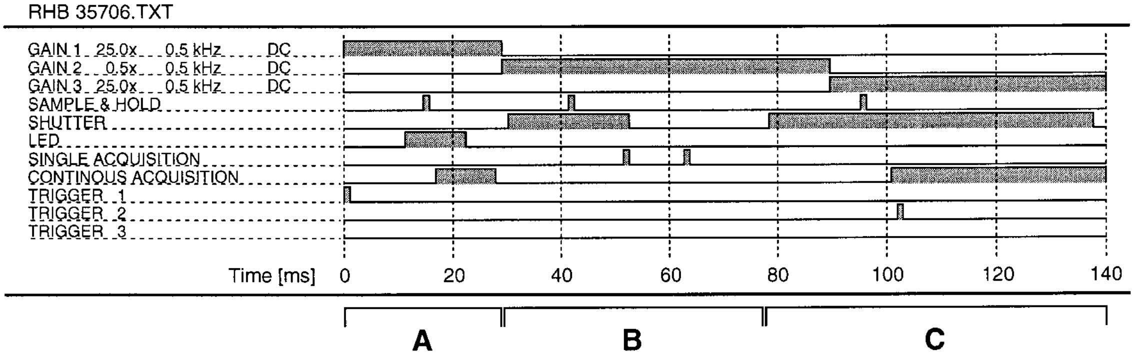

FIGURE 3 Time diagram of the settings of the recording system as generated for each experiment by the data acquisition program. The protocol for this particular experiment lasted for 140 ms and can be divided into three phases, which are explained in more detail in the text. Phase A: Test of the frequency response of the amplifiers with the aid of an LED pulse. Phase B: Determination of the resting fluorescence. Phase C: Actual experiment.

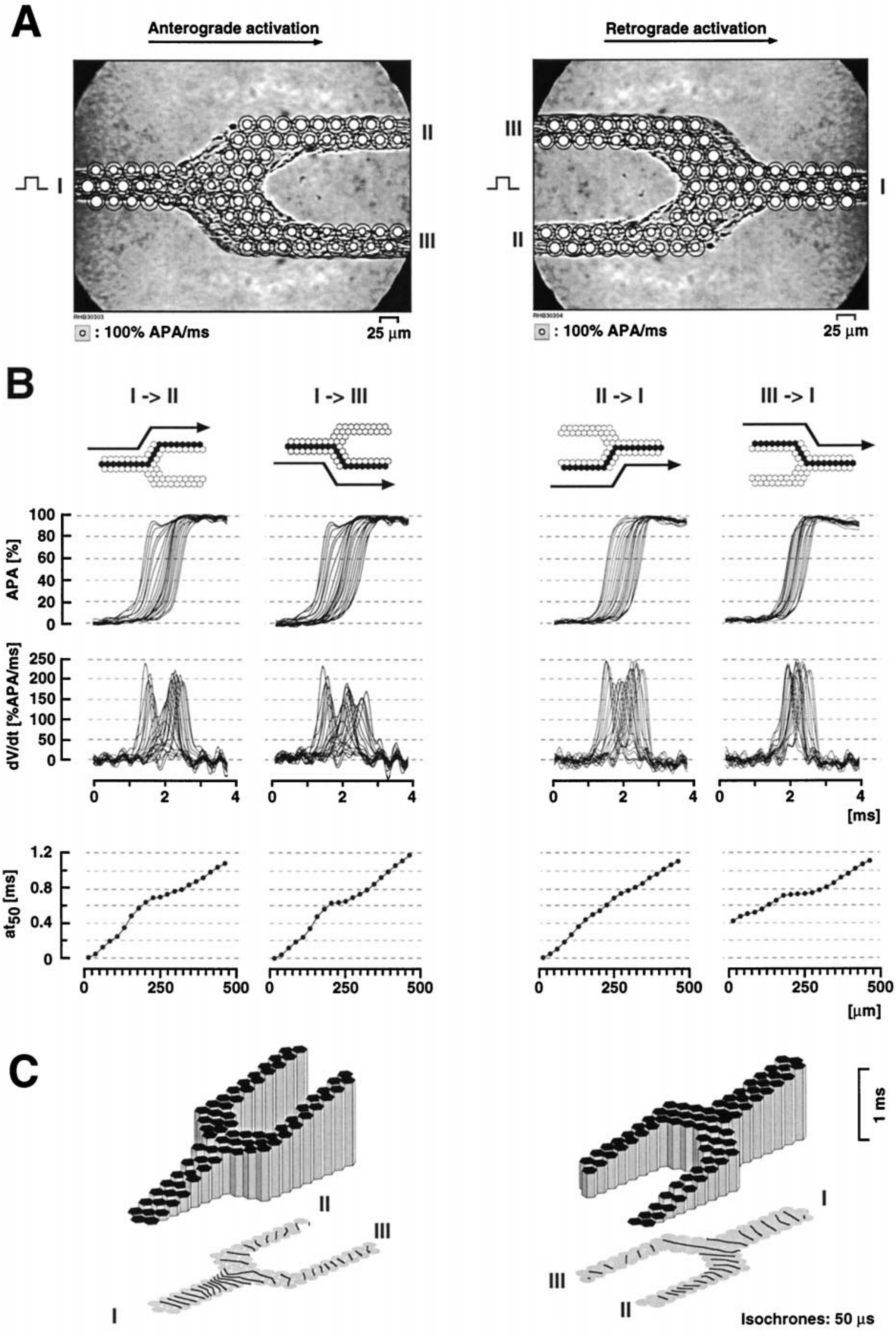
A
Anterograde activation
Retrograde activation
I
II
III
RHB30303
RHB30304
: 100% APA/ms
25 μm
B
I -> II
I -> III
II -> I
III -> I
APA [%]
dV/dt [%APA/ms]
[ms]
at50 [ms]
[μm]
0
2
4
250
500
C
1 ms
Isochrones: 50 μs

tailed picture of activation despite a limited number of detectors. The measurement was aimed at characterizing impulse propagation in a branching structure of cardiac tissue. This structure can be looked upon as a model for the terminal branching of Purkinje fibers, which has previously been shown to be a substrate for the generation of reentrant activity (Cranefield et al., 1973). The patterned growth culture consisted of a 60-μm-wide parent cell strand branching into two daughter strands of identical width. The preparation was stimulated either from the side of the parent strand (anterograde activation) or, simultaneously, from both daughter strands (retrograde activation). Fig. 4 *A* shows a videomicrograph of the preparation taken with the CCD camera equipped with the fiber optic taper. The arrangement of photodetectors is indicated by black circles, and maximum upstroke velocities (dV/dt_{max}) obtained at each recording site are indicated by white discs with a diameter proportional to dV/dt_{max}. The optically recorded upstroke portions of the propagating action potential are shown, separately for each daughter strand, in Fig. 4 *B* together with dV/dt and activation times along the preparation. The signals obtained during anterograde conduction (*two left columns*) showed the typical signs of a current-to-load mismatch (Rohr and Salzberg, 1994a). As the action potential reached the site of the bifurcation, i.e., the site of the increased load, it slowed down temporarily, and dV/dt_{max} was substantially reduced. The slowing of conduction was accompanied by bidirectional electrotonic interactions across the bifurcation, as evidenced by the shape of the action potential upstrokes in the parent strand. Initially, potentials did not reach full amplitude, and they showed an immediate and transient repolarization, which was reversed after the daughter strands were activated. The second transient decrease in upstroke velocities in daughter strand III was most likely due to a localized increase in axial resistance in this branch, the cause of which is unknown. During retrograde conduction (*two right columns*), which was elicited 2 mm from the recording site simultaneously in both daughter strands, propagation in strand III reached the recording area 0.5 ms later than that in strand II. Therefore, the activation wavefront in strand II was again confronted with a current-to-load mismatch similar to the situation described above for anterograde conduction. Accordingly, propagation temporarily slowed down, and dV/dt_{max} transiently decreased. In contrast, activation arriving with a delay from strand III was no longer faced with a current-to-load mismatch and, therefore, proceeded unhindered through the preparation. The absence of a transient increase in dV/dt_{max} in both strands in the region of the bifurcation suggests that the specific timing of the approaching wavefronts induced a facilitation of conduction in daughter strand III rather than a collision.

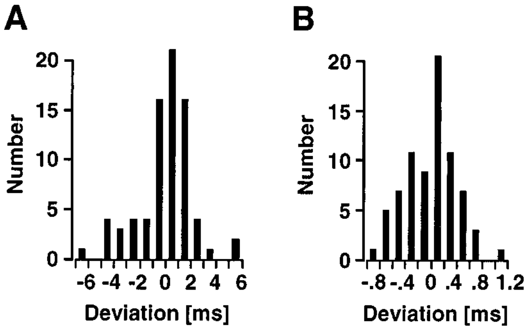

FIGURE 5 Histograms of the temporal deviations of the responses of all photodetectors to the falling edge of an LED pulse. (*A*) Distribution of temporal deviations of the raw signals (bin width 1 ms). (*B*) Distribution of temporal deviations after correction with a test LED pulse (bin width 0.2 ms). For further explanation see text.

Temporal accuracy of the recording system

As described in Materials and Methods, two measures were implemented to ensure that the system was capable of accurately tracking fast propagating events at the cellular/subcellular scale: 1) the bandwidths of all IVCs were fine-tuned to a similar frequency response (time constant of 100 μs; $f_o = 1.6$ kHz), and 2) all signals were simultaneously sampled. Based on these features, it was expected that temporal delays in the microsecond range could be detected between fast rising optical signals. This assumption was tested by applying a square LED pulse to the array and by determining at_{50} for each recording site. The results of such an experiment (Fig. 5 *A*) show that there remained a dispersion of at_{50} with a standard deviation of ± 2.1 μs (range -6 to 6 μs; $n = 75$), despite the measures taken. This dispersion was most likely due to variations in the specifications of electronic components "distal" to the IVCs. To compensate for this dispersion, a short LED pulse was routinely recorded with each experiment. This permitted the determination of the temporal deviation of each channel and, subsequently, the correction of the "real" activation times. Using this procedure on a LED pulse simulating an

FIGURE 4 Impulse propagation in a branching structure of cardiac tissue. (*A*) Videomicrograph of the preparation during anterograde (*left*) and retrograde (*right*) activation, with overlaid black circles indicating the positions of recording sites. The white discs inside the black circles represent a measure for dV/dt_{max} obtained at the respective locations (corresponding scale shown below picture). To simplify orientation in the preparation, the three branches are labeled I, II, and III. (*B*) Selection of signals recorded during anterograde (*two left columns*) and retrograde (*two right two columns*) propagation. The origins of the respective data are illustrated schematically at the top of each column. The signals of the paired columns were acquired simultaneously, but are split for reasons of clarity. (*Top row*) Action potential upstrokes versus time. (*Middle row*) First derivatives of upstrokes versus time. (*Bottom row*) Activation times versus distance. (*C*) Three-dimensional representation of activation times along the preparation (*top*) and corresponding isochrones of activation (*bottom*). The scale given on the right side of the panel applies to both graphs (*left*, anterograde activation; *right*, retrograde activation).

action potential upstroke, the standard deviation of activation times was reduced to ±0.4 μs ($n = 75$; range −0.8 to 1.2 μs; Fig. 5 *B*).

Based on these characteristics, it was expected that propagating events in the range of 1 m/s could be resolved with a spatial resolution of ≤10 μm. To test this prediction, a propagating light intensity change was simulated by placing a rotating steel blade (2000 rpm) in the object plane of a 20× objective and recording, in transillumination mode, the shuttering of the field of view. The result of such an experiment is illustrated in Fig. 6. Signals were recorded with the spatial arrangement of detectors shown in Fig. 6 *A*. Fig. 6 *B* depicts the isochrones of the light intensity change as the blade swept over the objective. The isochrones were parallel because the distance between the axis of rotation and the center of the objective (20 mm) was large compared to the diameter of the field of view (1 mm), which resulted in a virtually parallel shuttering of the recording area. Individual signals recorded along the center row of detectors are shown in Fig. 6 *C*. A linear fit of the at_{50} values of these signals yielded a velocity of the blade of 4.25 m/s, which was close to the theoretically predicted value of 4.19 m/s. From this finding, namely that a light intensity change propagating with a velocity of 4.25 m/s can be measured with a spatial resolution of 50 μm (20× objective), it can be inferred that the system is capable of tracking events propagating at up to 0.8 m/s with a spatial resolution of 10 μm or less, i.e., with cellular/subcellular resolution. Finally, if it is assumed that the signals shown in Fig. 6 *C* correspond to a transmembrane voltage change of 100 mV, the resulting maximum upstroke velocities as shown in Fig. 6 *D* would have been in the range of 500 V/s, which marks the highest possible frequency response of the recording system.

Determination of activation times and signal-to-noise ratios

Although the assessment of the temporal accuracy of the recording system as outlined in the previous paragraphs was performed with signals having a high SNR (rms), lower SNRs are to be expected in real experiments, especially at very low and very high magnifications, i.e., at low light levels. It is easily recognized that, even though the recording system is accurate to ±1 μs, any substantial noise added to the real signal can result in distortions of the determination of at_{50}. To characterize this dependence, real noise recordings were overlaid on a simulated "noiseless" action potential upstroke (both digitized at 20 kHz). The noise trace was then shifted in steps of 50 μs (i.e., one sample) along the signal for a total of 1000 steps, and the mean activation time ± SD was determined. This procedure was repeated for different SNRs by scaling the amplitude of the noise. Because activation times in optical recordings were determined in the past as either the moment of 50% depolarization (at_{50}) (Rohr and Salzberg, 1994b) or as the mo-

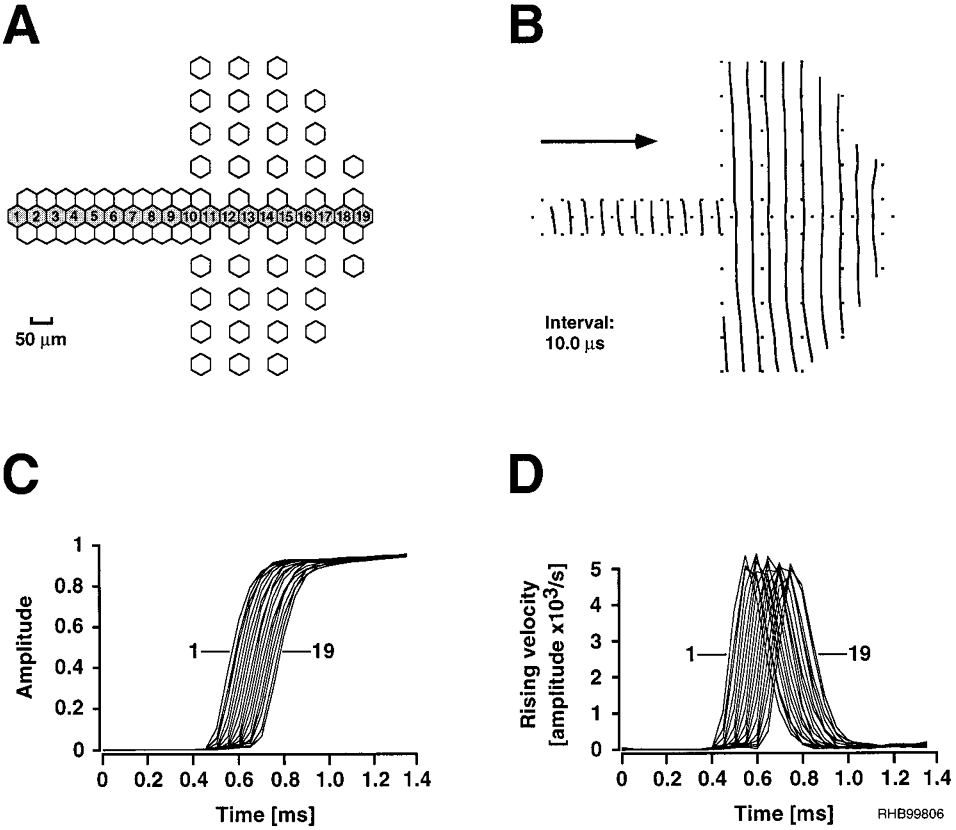

FIGURE 6 Mapping of the rotation of a steel blade in the object plane of the microscope (20× objective). (*A*) Spatial arrangement of the recording sites. (*B*) Isochrones indicating the sweeping of the edge of the blade across the field of view of the microscope. (*C*) "Action potential upstrokes," i.e., signals recorded at the numbered sites shown in *A* during the blockade of transmitted light by the advancing edge of the blade. (*D*) Time derivatives of the signals in *C*.

ment of occurrence of the maximum upstroke velocity ($at_{dV/dtmax}$) (Fast and Kleber, 1993), both types of determinations were simulated for comparison purposes. As shown in Fig. 7, either procedure yielded large errors in the determination of activation times at low SNRs. For the case of $at_{dV/dtmax}$ (Fig. 7 *A*), standard deviations smaller than 10 μs required SNRs of >50 for fast rising signals, whereas in the case of signals rising with a d*V*/dt_{max} of 50 V/s, even an excellent SNR of 600 resulted in errors of >30 μs in the determination of activation times. In contrast to the determination of activation times based on $at_{dV/dtmax}$, the use of at_{50} was more robust against noise present in the signals. Standard deviations smaller than 10 μs required SNRs of only 30 for fast rising signals, whereas in the case of slowly rising signals, the same accuracy could be obtained with SNRs below 100 (Fig. 7 *B*). These simulations illustrate that to profit from the high temporal accuracy of the recording system, SNRs should be in the range of 150 (fast rising signals) to 600 (slowly rising signals), and determinations of activation times should be based on at_{50} rather than $at_{dV/dtmax}$ for monotonically rising action potentials.

Spatial resolution of the recording system

With the system presented, it is theoretically possible to obtain optical recordings at spatial resolutions in the submicrometer range by combining optical fibers with a diameter of 100 μm or less with high magnification objectives. However, restraints from signal-to-noise considerations will limit the range of useful magnifications because, at both low magnification (objectives with small numerical apertures) and high magnification (small tissue areas), the fluorescence changes will be barely large enough to surpass the dark noise of the system. Therefore, both the photodiodes and the components of the IVCs were carefully selected to minimize this source of noise. When measured at full bandwidth (f_o = 1.6 kHz) and full gain (5 × 10^{10}), overall peak-to-peak (pp) dark noise as measured during a recording period of 10 ms amounted to 75 ± 25 mV (mean ± SD, $n = 75$). To determine experimentally the useful optical resolution, propagated action potentials were recorded in linear strands of myocytes (width 50–100 μm) at magnifications ranging from 5× to 250×. The results of these experiments are shown in Fig. 8. Although signals could be recorded at all magnifications corresponding to spatial resolutions ranging from 4 μm to 200 μm, signals at either extreme yielded poor SNRs of ~30 because, as outlined above, light levels and therefore signal amplitudes were minimal. Between these two extremes, objectives offering highly efficient light throughputs improved SNRs substantially. The highest values (between 200 and 300) could be recorded with the 40× objective, as illustrated by the example shown in Fig. 8 *D*. During experiments using objectives with a large light throughput, the predominant source of noise changed from dark noise to noise caused mainly by the small ripple of the light source (<0.1%). These experiments illustrate that the recording system is capable of resolving transmembrane voltage changes with spatial resolutions ranging from the subcellular to the multicellular level.

Accuracy of optical determinations of d*V*/dt_{max}

As evidenced by the table in Fig. 8 *H*, maximum upstroke velocities had the tendency to increase with increasing optical magnifications. Although it cannot be entirely excluded that this effect was partly due to variations in the electrophysiological characteristics of the different preparations, the pairing of the highest conduction velocities (44 cm/s) with both low d*V*/dt_{max} (77% APA/ms) at low magnification and high d*V*/dt_{max} (112% APA/ms) at high magnification suggests that the optical recording itself was

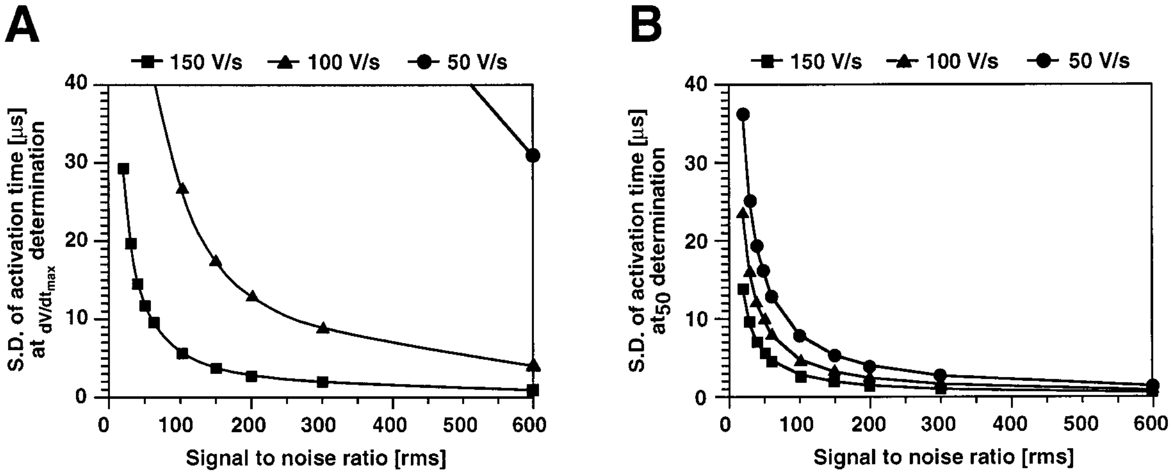

FIGURE 7 Dependence of the accuracy of determinations of activation times on signal-to-noise ratios (SNRs). (*A*) Standard deviation of activation times determined from the point in time of occurrence of the maximum upstroke velocity, $at_{dV/dtmax}$, as a function of SNR ($n = 100$). The three curves were obtained for different maximum upstroke velocities (■, 150 V/s; ▲, 100 V/s; ●, 50 V/s). (*B*) Same as in *A*, except that activation times were obtained from the point in time of 50% depolarization, at_{50}.

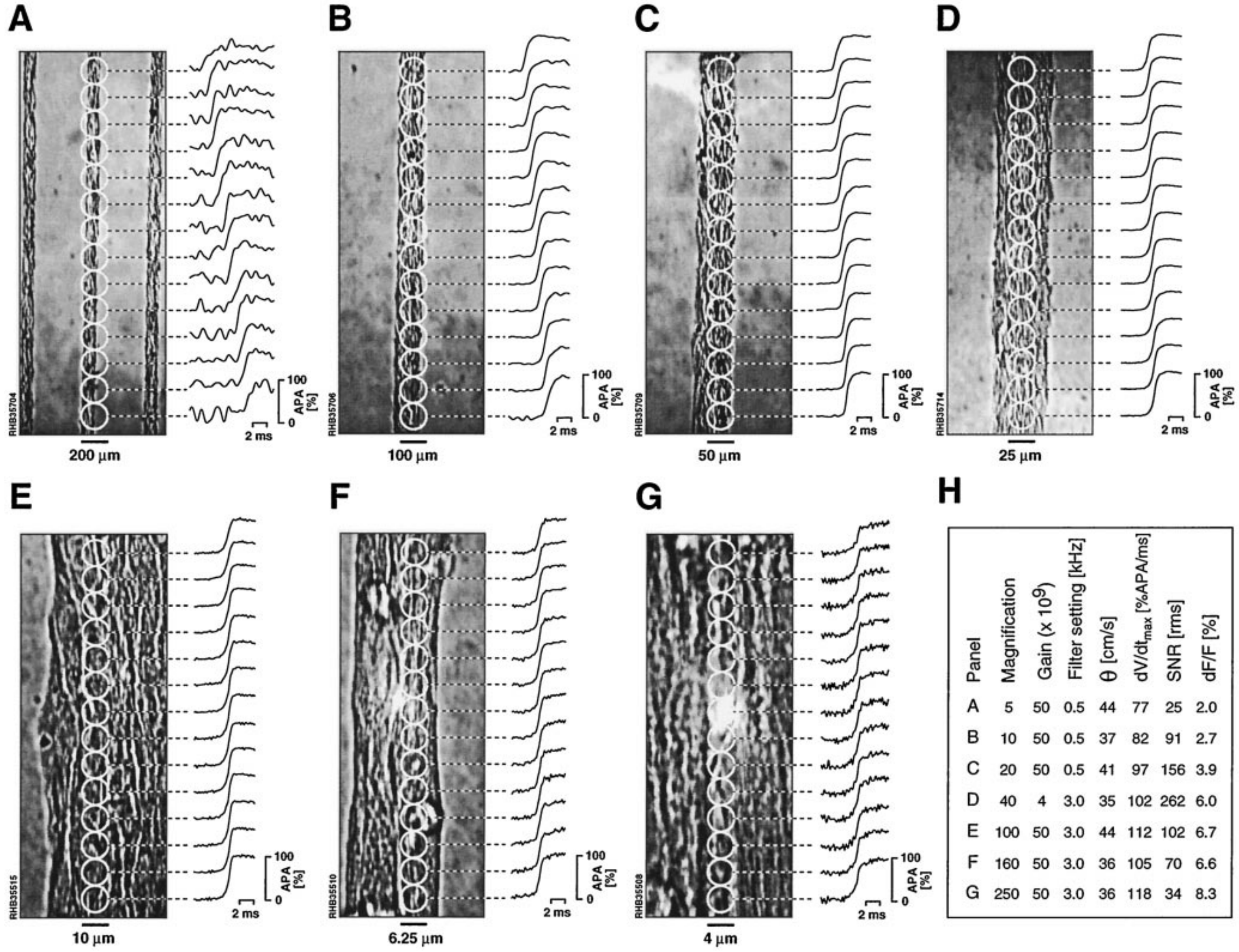

Panel	Magnification	Gain (x 10^9)	Filter setting [kHz]	θ [cm/s]	dV/dt$_{max}$ [%APA/ms]	SNR [rms]	dF/F [%]
A	5	50	0.5	44	77	25	2.0
B	10	50	0.5	37	82	91	2.7
C	20	50	0.5	41	97	156	3.9
D	40	4	3.0	35	102	262	6.0
E	100	50	3.0	44	112	102	6.7
F	160	50	3.0	36	105	70	6.6
G	250	50	3.0	36	118	34	8.3

FIGURE 8 Optical determination of impulse propagation along linear strands of patterned growth heart cells (widths 20–100 μm) at different spatial resolutions. The white circles overlaid on each photograph indicate recording sites along the strands ($n = 14$ each). The preparations were stimulated at a basic cycle length of 500 ms on top (outside the field of view), and the upstrokes of the propagating action potentials are shown to the right of each photograph. The spatial resolution is indicated by the bar below each photograph. Optical magnifications were 5× (*A*), 10× (*B*), 20× (*C*), 40× (*D*), 100× (*E*), 160× (*F*) and 250× (*G*). Conduction velocities (θ), maximum upstroke velocities (dV/dt_{max}), signal-to-noise ratios (SNRs), and fractional fluorescence changes (dF/F) for each magnification are summarized by the table in *H*.

responsible for the variations in dV/dt_{max}. At low spatial resolutions, optical recordings of transmembrane voltage represent the sum of upstrokes recorded from many cells. Whereas in the theoretical case of a simultaneous excitation of all cells recorded by a single photodetector, the determination of dV/dt_{max} should not deviate from the real value, this is not the case if activation propagates: the summing characteristics of the optical recording will, in this case, tend to spatially average action potential upstrokes arising from sequentially activated cells and, therefore, result in an underestimation of the true values. Obviously, this effect is expected to increase with both decreasing magnification and decreasing conduction velocity. Fig. 9 shows the results of a simulation aimed at the characterization of this dependence: the optically recorded dV/dt_{max} of a continuously propagating action potential with a constant dV/dt_{max} of 100 V/s is displayed as a function of the conduction velocity and of the magnification used. As expected, the curves for the lowest magnification showed the largest depression of the recorded dV/dt_{max} value because averaging occurred over a large distance. On the other hand, when the 100× objective was simulated (trace 10), deviations from the real dV/dt_{max} became obvious only at highly reduced conduction velocities. These results suggest that, during fast and continuous conduction, optically measured dV/dt_{max} closely reflect real values, whereas at slow conduction velocities and small magnifications, the optically determined values are likely to represent an underestimation.

Motion artifact subtraction

Optical measurements of transmembrane voltage changes in contractile tissues have the disadvantage that the contrac-

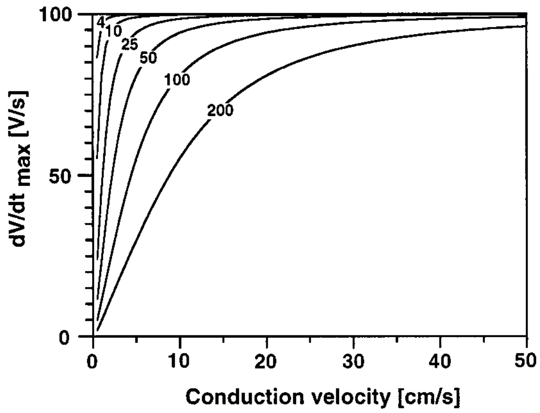

FIGURE 9 Dependence of the accuracy of optical determinations of dV/dt_{max} on conduction velocities: propagating action potentials with a constant dV/dt_{max} of 100 V/s were simulated, and the optically determined compound upstroke velocity, at a given spatial resolution (*numbers in curves*, μm), was calculated as a function of conduction velocity. With decreasing conduction velocity, optically measured maximum upstroke velocities led to an increasing underestimate of dV/dt_{max}. Whereas at very high magnifications this effect was negligible, the error was substantial at low to intermediate resolutions and low conduction velocities.

tion-induced light scattering distorts the shape of the action potentials. Although this distortion does not affect the action potential upstroke because of the latency of onset of contraction, it tends to deform the repolarization phase substantially. This deformation is especially pronounced if the region monitored by a given detector contains brightly stained debris that adheres to the cell monolayer and therefore moves with every contraction. Because it has been shown that the emission spectrum of the voltage-sensitive dye di-4-ANEPPS, a close analog to di-8-ANEPPS, contains two distinct regions reacting with either a decrease (longer wavelengths) or an increase (shorter wavelengths) in fluorescence intensity to depolarizations of the membrane (Fromherz and Lambacher, 1991), it seemed feasible to use a dual-emission wavelength approach to correct optically for motion artifacts. The result of such an experiment is illustrated in Fig. 10. The preparations were broadly excited (excitation: <500 nm; dichroic mirror: 505 nm; emission: >515 nm), and the emitted light was split by a dichroic mirror (590 nm) and directed to the two matching fiber optic arrays attached to the OC (cf. Fig. 1). Accordingly, one array recorded light with wavelengths of >600 nm (Fig. 10 *B*), and the other received light with wavelengths between 515 and 590 nm (Fig. 10 *C*). As expected, di-8-ANEPPS reacted with opposite changes in fluorescence to the change in membrane potential, as indicated by action potential upstrokes going up (Fig. 10 *B*) or down (Fig. 10 *C*). Signals recorded at either wavelength showed a considerable distortion of the action potential due to the motion artifact. This distortion was completely eliminated after subtraction of the signals in Fig. 10 *C* from those in Fig. 10 *B* (Fig. 10 *D*). Action potential durations determined from the set of traces in Fig. 10 *D* were 78 ± 10 ms (average ± SD, $n = 19$) at 80% of full repolarization and are similar to values determined earlier using intracellular electrodes in cultures of the same age (6 days; 85 ms; Rohr et al., 1991). In addition to correction of motion artifacts, dual-emission wavelength measurements also tended to increase the SNR because the signal sizes and the level of common mode noise rejection were increased. These results illustrate that it is feasible to record optically, with cellular resolution, spatial patterns of action potential repolarization without using drugs that might interfere with the normal electrophysiological characteristics of the tissue.

DISCUSSION

The precise optical characterization of excitation patterns arising in networks of excitable cells at a microscopic scale requires transmembrane voltage changes to be recorded at high spatial and temporal resolution. In this context, we presented a recording system that 1) has an open architecture, permitting an effortless upgrading of the number of available detectors; 2) permits the spatial arrangement of recording sites to be adjusted according to regions of interest; and 3) has a temporal resolution that permits the resolution of events separated by a few microseconds during single-shot experiments.

Spatial resolution and noise performance

Relaying the microscopic image by a flexible fiber optic assembly to individual detectors has four main advantages over conventional systems using fixed photodiode arrays or CCD cameras as detectors:

1. The useful spatial resolution is not limited by the physical dimensions of the actual photodetector, but is defined solely by the diameter of the individual optical fibers, by the optical magnification used, and by signal-to-noise considerations. It is therefore theoretically possible to extend the resolution into the submicrometer range by using smaller fiber diameters and quieter detectors.

2. The possibility of rearranging the spatial pattern of detectors has the unique advantage that the location of recording sites can be adjusted to regions of interest in a given preparation, thereby circumventing the problem of “wasted” photodetectors. This possibility was particularly helpful when electrical activity was determined in narrow linear preparations stretching across the entire field of view. In these cases, the adjustment of the detector layout to the shape of the preparation allowed conduction to be mapped, despite a limited number of photodetectors, with a resolution that could have been achieved only with the highest resolution photodiode array commercially available (22 × 22 diodes; Falk et al., 1993).

3. Because the photodetectors are not committed, it is possible to assign individual detectors to different ports of the microscope, thus enabling dual-emission wavelength measurements. In addition, it is possible to simultaneously monitor other parameters relevant for the experiment, such

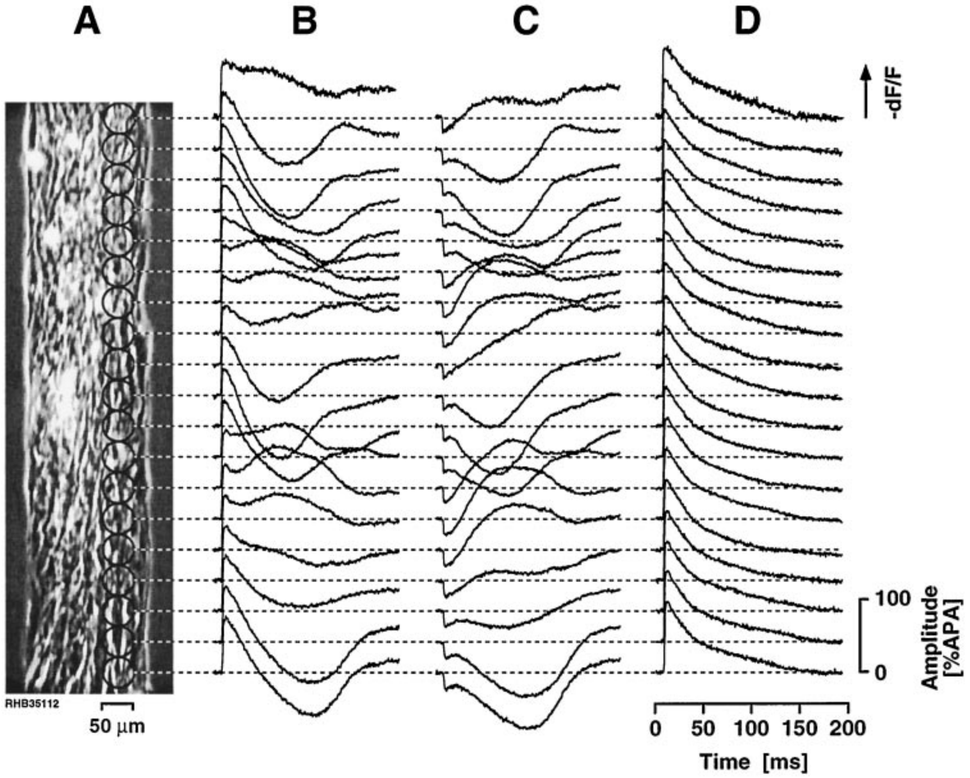

FIGURE 10 Motion artifact subtraction by simultaneous dual-emission wavelength measurements. (*A*) Phase-contrast videomicrograph of the preparation, which consisted of a 180-μm-wide cell strand (overall length 1 cm). The overlaid black circles correspond to the locations imaged simultaneously by two image conduits at two different emission wavelengths. (*B*) Compound signals (transmembrane voltage change plus motion artifact) recorded at an emission wavelength of >600 nm. The signals are scaled to resting fluorescence. Following the normal convention, a decrease in fluorescence is shown as a positive signal. The repolarization is grossly distorted in all traces because of contraction-induced light scattering and the movement of adherent fluorescent particles. (*C*) Compound signals recorded at an emission wavelength $515 \text{ nm} < x < 590 \text{ nm}$ (signals scaled to resting fluorescence). In contrast to *B*, upstrokes are negative because of the increase in fluorescence, whereas the contraction-induced distortions have identical polarities. (*D*) Subtraction of the signals in *C* from the corresponding signals in *B* yields action potential shapes that are devoid of the motion artifact (action potential amplitudes scaled to 100%).

as light intensity fluctuations at the lamp housing, which might serve to correct the optical signals for light ripple or arc drift.

4. Using discrete photodetectors permits the most appropriate types of photodiodes to be selected during construction. Furthermore, the modular arrangement of detectors and their electronics on printed circuit boards connected to a proprietary bus permits the straightforward upgrade of the number of detectors without having to make any changes to the other components of the system.

The disadvantages of the fiber optic imager compared to conventional systems are twofold. First, the rearrangement of fibers took, in the case of a random selection of 80 of 379 fibers, between 20 and 30 min to complete. Whereas this did not pose a problem for patterned growth preparations, where the shape of the preparations remained the same for the whole series of experiments, the rearrangement might be too cumbersome in the case of frequently changing tissue geometries. In this case, it would be possible to equip all fibers with IVCs and then switch signals of interest electronically to the analog signal conditioning circuitries and the ADCs. Second, in contrast to direct imaging devices like photodiode arrays, optical signals underwent attenuation during their passage through the optical fibers (<20%, data not shown). Because, at the length of the fibers used (60 cm), attenuation caused by the medium itself is less than 1% at 650 nm (specifications from the manufacturer), most of this light loss presumably occurred at the interfaces of the fiber optic cables, i.e., at the passage of light into and out of the fiber. Although this attenuation is not very large, it nevertheless compromised SNRs slightly.

Useful spatial resolutions obtained with the recording system ranged from 4 μm to 200 μm. Signal-to-noise ratios were small at either extreme because of low light levels. At low magnification (200 μm), this was primarily due to the small numerical aperture of the objective (signal size is approximately proportional to the fourth power of N.A.; Ratzlaff and Grinvald, 1991), whereas, at high magnification (4 μm), light intensities were low because of the small size of the area imaged. At both extremes of magnification, measurements were limited by the noise arising from the amplifiers (dark noise). In the case of sufficiently quiet amplifiers, this noise current is dominated by the Johnson noise (i_J) arising from the feedback resistor (R_f), $i_J =$

$(4kTB/R_f)^{1/2}$, where k is the Boltzmann constant, T is the absolute temperature, and B is the bandwidth (Horowitz and Hill, 1989). In the case of our system ($B = 1.6$ kHz, $R_f = 10^8\ \Omega$), the noise current amplitude predicted from this formula is 510 fA rms. By careful selection of the components of the first stage (photodiodes and IVCs), the system specifications could be kept close to this theoretical limit (mean dark current amplitude of 900 fA rms).

Temporal precision

Because the system was built with the goal of measuring impulse propagation on a subcellular scale, it was imperative that the system have a sufficiently high bandwidth to resolve fast rising signals, that the bandwidths of all detectors were identical, and that all of the signals were acquired simultaneously. These requirements were met by using moderately sized feedback resistors in the IVCs, by fine-tuning the bandwidth of this stage, and by introducing S&H amplifiers in front of the analog-to-digital converters. These measures resulted in a dispersion of activation times recorded by the detectors of a few microseconds, which was further reduced to $\pm 1\ \mu$s by applying a digital correction based on a LED test pulse. This feature permitted the determination of temporal delays among fast rising signals that were shorter than the conversion period of the analog-to-digital converters, as illustrated by the imaging of a fast rotating shutter. In this experiment, activation delays between neighboring detectors amounted to $11.6 \pm 1.1\ \mu$s (mean ± SD, $n = 18$), i.e., it was possible to pinpoint the signal caused by the blade with an uncertainty of $\pm 1.1\ \mu$s, even though the conversion period amounted to 50 μs.

Although the blade experiments illustrated the temporal response characteristics of the system at very high SNR, fluorescence signals from cells generally exhibit lower SNRs, and consequently, temporal precision will be compromised by noise. The dependence of the accuracy of determinations of $at_{\mathrm{dV/dtmax}}$ on SNRs for the case of a signal rising with a fixed upstroke velocity has been simulated before (Fast and Kleber, 1993). Here we extended these simulations to show that the accuracy of the determination of activation times is additionally dependent on the mode of their assessment (at_{50} or $at_{\mathrm{dV/dtmax}}$) and on the values of the maximum upstroke velocities themselves. The simulations showed that determinations of activation time based on at_{50} are less noise dependent than those based on $at_{\mathrm{dV/dtmax}}$, and that errors in the determination of activation times tend to increase with decreasing upstroke velocities. If the best SNRs reported in this study (SNR rms = 262) are taken as reference, the dispersion of activation delays for signals rising with 100 V/s amounts to 11 μs ($at_{\mathrm{dV/dtmax}}$) and 2 μs (at_{50}). This difference in the accuracy of the determination between the two modes of calculation is readily explained by the high susceptibility of $at_{\mathrm{dV/dtmax}}$ to spurious noise in the signal and it suggests that, for optical recordings, at_{50} should be given preference for the determination of activation under conditions of continuous conduction. While in general, errors in the determination of activation times can be neglected at low magnifications, where they represent only a small fraction of the overall activation delay between neighboring detectors, they have to be taken into consideration at higher magnifications, where they might cause a significant distortion of the activation pattern.

Optical determination of d*V*/d*t*$_{\mathrm{max}}$

The accuracy of optical determinations of dV/dt_{max} is determined by five factors: 1) the estimate of the true action potential amplitude, 2) the frequency response of the indicator, 3) the frequency response of the recording system, 4) the SNR, and 5) spatial averaging effects. In the following, the contribution of each of these factors is discussed separately:

1. Because single-wavelength optical measurements of transmembrane voltage only yield relative values for action potential amplitudes (APAs), the arbitrary assignment of absolute values to the signal amplitudes results in errors in dV/dt_{max} determinations equal to the percentage error of the APA estimates.

2. The voltage-sensitive dye di-8-ANEPPS belongs to the class of fast indicators, which have been shown to respond within microseconds to changes in transmembrane voltage (Salzberg et al., 1993). This suggests that the dye does not limit the determination of dV/dt_{max}.

3. As shown by the rotating blade experiments, the frequency response of the system ($f_o = 1.6$ kHz) allowed upstroke velocities as fast as 500 V/s to be recorded. Because upstroke velocities normally encountered in cultured heart cells are in the range of 100–200 V/s, the bandwidth of the system does not significantly limit the optically measured upstroke.

4. Because shot noise and noise arising from the electronic circuitry have a bandwidth equal to the overall bandwidth of the system, dV/dt_{max} determinations at low SNRs are prone to representing an overestimate. Simulations of the dependence of dV/dt_{max} on SNR illustrated that this overestimate for an unfiltered signal rising with 100 V/s increases from 0% to 20% with SNRs that decrease from 150 to 25 (same type of simulation as used for assessing the influence of SNR on the determination of activation times; data not shown).

5. Finally, optical determinations of dV/dt_{max} during a propagated activation can be falsely low because of spatial averaging effects: if a given detector receives input from several sequentially activated cells, the overall signal represents a compound signal that rises more slowly than the action potential upstrokes from the individual cells. This effect, which was referred to previously as “blurring artifact” (Girouard et al., 1996), can lead to substantial artifactual reductions in dV/dt_{max}. Summarizing all effects, errors in dV/dt_{max} estimates in optical recordings of action potentials propagating uniformly at velocities of >20 cm/s, at intermediate to high magnifications and under conditions of

SNR > 100, are nearly exclusively determined by the error of the estimate of the action potential amplitude. On the other hand, if lower magnifications are used or if conduction is slow or discontinuous, spatial averaging can result in an underestimate of dV/dt_{max}.

Fast dual-emission measurements

Optical recordings in contractile tissues have the disadvantage that the contraction itself causes fluctuations in the light intensity, which distorts the repolarization phase. In the past, three main strategies were applied to overcome this disadvantage: 1) motion was minimized by pressing the tissue against a glass window (Rosenbaum et al., 1991; Kanai and Salama, 1995; Girouard et al., 1996); 2) for experiments in which the length but not the actual shape of the repolarization phase mattered, the end of repolarization was elegantly identified by a maximum in the second derivative of the optical signal (Efimov et al., 1994); 3) undisturbed visualization of the repolarization phase was achieved by suppressing contraction with suitable drugs, such as butanedionemonoxime (Pertsov et al., 1993; Gray et al., 1995) or verapamil (Dillon, 1991; Kwaku and Dillon, 1996). Unfortunately, both of these drugs have side effects at the concentrations used to suppress contraction. Butanedionemonoxime ($\geq$10 mM) was shown to affect various transmembrane currents (I_{Ca}, I_{to}; Coulombe et al., 1990; Chapman, 1993), and calcium channel blockers can directly affect impulse propagation (Rohr and Kucera, 1997). As an alternative to these approaches, the present study shows that motion artifacts can be completely eliminated by a single-fluorophore/dual-emission wavelength protocol. This technique permits the spatially resolved visualization of action potential repolarization without the use of contraction-suppressing drugs. The success of this approach was critically dependent on two prerequisites: 1) Signals at the different wavelengths had to be recorded simultaneously. If signals were acquired sequentially after switching of emission filters, the elimination of the artifact was often incomplete, probably because of beat-to-beat fluctuations in the contraction signal. 2) The two fiber optic image conduits had to be precisely aligned to ensure that they were recording from exactly matching positions in the preparations. Errors in alignment as small as a few percent of the fiber diameter gave rise to highly incomplete eliminations of motion artifacts.

CONCLUSIONS AND PERSPECTIVES

Because of its modular design, the optical recording system presented offers a flexible approach to the spatially resolved measurement of fast optical signals with subcellular resolution, which can be easily upgraded in terms of the number of photodetectors. The use of an exchangeable fiber optic image conduit between the microscope and the detectors opens the possibility of designing higher resolution imagers by using smaller fiber diameters and/or two or more fiber optic arrays to simultaneously record signals at different emission wavelengths. Furthermore, the fiber optics make it feasible to extend the capabilities of the system into the macroscopic range, not only by replacing the microscope with a tandem-lens macroscope (Ratzlaff and Grinvald, 1991), but by placing the fiber inputs directly in contact with a given preparation. As an example, it should be possible to shape the optical front end in such a way as to form a hollow cylinder in which the whole surface of a papillary muscle could be placed and imaged simultaneously in three dimensions. In such an experiment, part of the fibers could be assigned to delivering the excitation light to the preparation, and the other fibers could be used to record from the tissue in a manner similar to that of the "optrode" design described earlier (Dillon, 1991; Neunlist et al., 1992; Witkowski et al., 1994). Furthermore, the sensitivity of the system could be increased by replacing the photodiode detectors with devices offering less dark noise at comparable gains, i.e., with photomultipliers or avalanche photodiodes. These devices could be inserted between the outputs of the fiber optic array and the integrators, thereby still making use of both the fiber optic input and simultaneous digitization capabilities of the system. Such an approach would possibly extend the range of useful resolutions at both smaller and larger magnifications than the ones currently used, and moreover, it would permit weaker signals to be recorded from other types of optical indicators.

We are greatly indebted to Peter Frei, Denis De Limoges, and H.-U. Schweizer for their technical assistance; to Regula Flückiger Labrada for the preparation of the cell cultures; and to Dr. H. P. Clamann for reading the manuscript.

REFERENCES

Chapman, R. A. 1993. The effect of oximes on the dihydropyridine-sensitive Ca current of isolated guinea-pig ventricular myocytes. *Pflügers Arch.* 422:325–331.

Chien, C. G., and J. Pine. 1991. An apparatus for recording synaptic potentials from neuronal cultures using voltage-sensitive fluorescent dyes. *J. Neurosci. Methods.* 38:93–105.

Coulombe, A., I. A. Lefevre, E. Derroubaix, D. Thuringer, and E. Coraboeuf. 1990. Effect of 2,3-butanedione 2-monoxime on slow inward and transient outward currents in rat ventricular myocytes. *J. Mol. Cell. Cardiol.* 22:921–932.

Cranefield, P. F., A. L. Wit, and B. F. Hoffman. 1973. Genesis of cardiac arrhythmias. *Circulation.* 47:190–204.

Dillon, S. M. 1991. Optical recordings in the rabbit heart show that defibrillation strength shocks prolong the duration of depolarization and the refractory period. *Circ. Res.* 69:842–869.

Efimov, I. R., D. T. Huang, J. M. Rendt, and G. Salama. 1994. Optical mapping of repolarization and refractoriness from intact hearts. *Circulation.* 90:1469–1480.

Falk, C. X., J. Z. Wu, L. B. Cohen, and A. C. Tang. 1993. Nonuniform expression of habituation in the activity of distinct classes of neurons in the *Aplysia* abdominal ganglion. *J. Neurosci.* 13:4072–4081.

Fast, V. G., and A. G. Kleber. 1993. Microscopic conduction in cultured strands of neonatal rat heart cells measured with voltage-sensitive dyes. *Circ. Res.* 73:914–925.

Fromherz, P., and A. Lambacher. 1991. Spectra of voltage-sensitive fluorescence of styryl-dye in neuron membrane. *Biochim. Biophys. Acta.* 1068:149–156.

Girouard, S. D., K. R. Laurita, and D. S. Rosenbaum. 1996. Unique properties of cardiac action potentials recorded with voltage-sensitive dyes. *J. Cardiovasc. Electrophysiol.* 7:1024–1038.

Gray, R. A., J. Jalife, A. Panfilov, W. T. Baxter, C. Cabo, J. M. Davidenko, and A. M. Pertsov. 1995. Nonstationary vortexlike reentrant activity as a mechanism of polymorphic ventricular tachycardia in the isolated rabbit heart. *Circulation.* 91:2454–2469.

Grinvald, A., D. Frostig, E. Lieke, and R. Hildesheim. 1988. Optical imaging of neuronal activity. *Physiol. Rev.* 68:1285–1366.

Hirota, A., K. Sato, Y. Momose-Sato, T. Sakai, and K. Kamino. 1995. A new simultaneous 1020-site optical recording system for monitoring neural activity using voltage-sensitive dyes. *J. Neurosci. Methods.* 56: 187–194.

Horowitz, P., and W. Hill. 1989. The Art of Electronics. Cambridge University Press, Cambridge.

Iijima, T., M. P. Witter, M. Ichikawa, T. Tominaga, R. Kajiwara, and G. Matsumoto. 1996. Entorhinal-hippocampal interactions revealed by real-time imaging. *Science.* 272:1176–1179.

Kamino, K. 1991. Optical approaches to the ontogeny of electrical activity and related functional organization during early heart development. *Physiol. Rev.* 71:53–91.

Kanai, A., and G. Salama. 1995. Optical mapping reveals that repolarization spreads anisotropically and is guided by fiber orientation in guinea pig hearts. *Circ. Res.* 77:784–802.

Kwaku, K. F., and S. M. Dillon. 1996. Shock-induced depolarization of refractory myocardium prevents wave-front propagation in defibrillation. *Circ. Res.* 79:957–973.

Neunlist, M., S. Z. Zhou, and L. Tung. 1992. Design and use of an “optrode” for optical recordings of cardiac action potentials. *Pflügers Arch.* 420:611–617.

Pertsov, A. M., J. M. Davidenko, R. Salomonsz, W. T. Baxter, and J. Jalife. 1993. Spiral waves of excitation underlie reentrant activity in isolated cardiac muscle. *Circ. Res.* 72:631–650.

Ratzlaff, E. H., and A. Grinvald. 1991. A tandem-lens epifluorescence macroscope: hundred-fold brightness advantage for wide-field imaging. *J. Neurosci. Methods.* 36:127–137.

Rohr, S. 1986. Temperature-controlled perfusion chamber suited for mounting on microscope stages. *J. Physiol. (Lond.).* 378:90p.

Rohr, S. 1995. Determination of impulse conduction characteristics at a microscopic scale in patterned growth heart cell cultures using multiple site optical recording of transmembrane voltage. *J. Cardiovasc. Electrophysiol.* 6:551–568.

Rohr, S., and J. P. Kucera. 1997. Involvement of the calcium inward current in cardiac impulse propagation: induction of unidirectional conduction block by nifedipine and reversal by Bay K 8644. *Biophys. J.* 72:754–766.

Rohr, S., and B. M. Salzberg. 1994a. Characterization of impulse propagation at the microscopic level across geometrically defined expansions of excitable tissue: multiple site optical recording of transmembrane voltage (MSORTV) in patterned growth heart cell cultures. *J. Gen. Physiol.* 104:287–309.

Rohr, S., and B. M. Salzberg. 1994b. Multiple site optical recording of transmembrane voltage in patterned growth heart cell cultures: assessing electrical behavior, with microsecond resolution, on a cellular and subcellular scale. *Biophys. J.* 67:1301–1315.

Rohr, S., D. M. Schölly, and A. G. Kleber. 1991. Patterned growth of neonatal rat heart cells in culture. Morphological and electrophysiological characterization. *Circ. Res.* 68:114–130.

Rosenbaum, D. S., D. T. Kaplan, A. Kanai, L. Jackson, H. Garan, R. J. Cohen, and G. Salama. 1991. Repolarization inhomogeneities in ventricular myocardium change dynamically with abrupt cycle length shortening. *Circulation.* 84:1333–1345.

Salzberg, B. M., A. L. Obaid, and F. Bezanilla. 1993. Microsecond response of a voltage-sensitive merocyanine dye: fast voltage-clamp measurements on squid giant axon. *Jpn. J. Physiol.* 43:37–41.

Witkowski, F. X., R. Plonsey, P. A. Penkoske, and K. M. Kavanagh. 1994. Significance of inwardly directed transmembrane current in determination of local myocardial electrical activation during ventricular fibrillation. *Circ. Res.* 74:507–524.